45th AIAA Aerospace Sciences Meeting, 8-11 Jan. 2007, Reno NV

Numerical Simulation of DC and RF Glow Discharges

Jonathan Poggie*

Air Force Research Laboratory, Wright-Patterson AFB, OH 45433-7512 USA

As part of an ongoing research effort on plasma actuators for flow control, a numerical study of DC glow discharges and γ-mode RF glow discharges has been carried out. For simplicity, the study focused on two-dimensional problems. Several experimentally observed features of these discharges were reproduced in the numerical computations, including the expansion of the electrode spot with increasing discharge current. The current results provide a basic validation of the computer code, but detailed experimental data are needed for true code validation.

I. Introduction

Since the mid-1990s, there has been considerable research interest in plasma-based flow control techniques for aerospace applications. Because of the weight and power consumption penalties of large-scale systems, small-scale actuators based on glow and arc discharges have become increasingly popular, and much effort has been put toward numerical modeling of the actuator behavior.

Relatively little effort, however, has been put into verification and validation of these codes. The coupling of fluid dynamics and electromagnetic effects leads to rather complex physical and numerical models, which demand careful testing, but relatively little suitable experimental data is available for comparison.

Nevertheless, grid resolution studies, code comparisons, and qualitative verification of basic physical phenomena are feasible. This paper makes a step in this direction by examining the normal current density effect that has been observed experimentally in DC and RF glow discharges, and reproduced in a few numerical studies.[1,2] Careful attention is paid to grid resolution. For simplicity, this initial effort focuses on two-dimensional problems.

II. Methods

A three-dimensional computer code has been written to solve the problem of a glow discharge actuator embedded in a high-speed fluid flow.[3,4] Here, a subset of the code's capability will be described, the part relevant to modeling a discharge in a quiescent gas in the absence of an applied magnetic field.

A. Physical Model

Assuming the absence of bulk gas flow and an applied magnetic field, we use the following drift-diffusion model in the present work:

$$\frac{\partial n_i}{\partial t} + \nabla \cdot \mathbf{\Gamma}_i = \alpha \Gamma_e - \beta n_i n_e \tag{1}$$

$$\frac{\partial n_e}{\partial t} + \nabla \cdot \mathbf{\Gamma}_e = \alpha \Gamma_e - \beta n_i n_e \tag{2}$$

where the species fluxes are given by:

$$\mathbf{\Gamma}_i = n_i \mu_i \mathbf{E} - D_i \nabla n_i \tag{3}$$

$$\mathbf{\Gamma}_e = -n_e \mu_e \mathbf{E} - D_e \nabla n_e \tag{4}$$

*Senior Aerospace Engineer, AFRL/VAAC, Bldg. 146 Rm. 225, 2210 Eighth St. Associate Fellow AIAA.

The electric potential is determined from the Poisson equation:

$$\nabla^2\phi = -e(n_i - n_e)/\epsilon_0 \tag{5}$$

where ϵ_0 is the permittivity of free space, and the electric field is found from $\mathbf{E} = -\nabla\phi$.

Gas heating was accounted for using the steady-state heat conduction equation:

$$-\nabla\cdot(\lambda\nabla T) = \eta\langle\mathbf{E}\cdot\mathbf{j}\rangle \tag{6}$$

where $\eta = 0.1$, $\mathbf{j} = e(\mathbf{\Gamma}_i - \mathbf{\Gamma}_e)$, and the angle brackets indicate averaging over one cycle of the forcing signal. (Equation (6) was implemented as a new module in the computer code.) The bulk gas pressure $p = Nk_BT$ was taken to be constant.

The calculations were carried out for nitrogen gas, with the following properties, obtained from Refs. 5,6. The ionization coefficient was $\alpha = \hat{p}A\exp(-B\hat{p}/E)$, where $A = 9.0$ (m·Pa)$^{-1}$, $B = 257$ V/m·Pa, $\hat{p} = pT_r/T$, and $T_r = 293$ K. The recombination coefficient was taken to be $\beta = 2\times10^{-13}$ m^3/s. The mobilities were $\mu_i = \mu_{ir}/\hat{p}$ and $\mu_e = \mu_{er}/\hat{p}$, where $\mu_{ir} = 19.2$ m^2/V·s·Pa and $\mu_{er} = 5900$ m^2/V·s·Pa. The corresponding diffusion coefficients were found from $D_i = \mu_i\, k_BT/e$ and $D_e = \mu_e\, k_BT_e/e$, where $T_e = 11600$ K. The thermal conductivity was computed from $\lambda = \lambda_r(T/T_r)^n$, where $\lambda_r = 0.242$ W/m·K, $n = 0.74$, and $T_r = 273$ K.

When the normal component of the electric field was directed away from an electrode (anode-like behavior), the normal component of the ion flux was assumed to be zero. For the opposite case of cathode-like behavior, the normal component of the electron flux was found from the relation $\mathbf{\Gamma}_e\cdot\mathbf{n} = -\gamma\mathbf{\Gamma}_i\cdot\mathbf{n}$, where γ is the secondary emission coefficient, $\mathbf{n}$ is a unit normal vector, and the species fluxes $\mathbf{\Gamma}_{i,e}$ were computed using one-sided, second-order spatial differences. For all the calculations reported in this paper, the value $\gamma = 0.1$ was assumed.

The potential at the right electrode was taken to be zero. The potential at the left electrode was determined by solving an auxiliary ordinary differential equation for the external circuit (see Fig. 1):

$$\dot{V} + V/(RC) = I/C \tag{7}$$

where

$$I = I_C + I_D = -\iint(\mathbf{j} + \epsilon_0\frac{\partial\mathbf{E}}{\partial t})\cdot\mathbf{n}\,dA \tag{8}$$

is the sum of the conduction and displacement currents at the right electrode in the plasma solution, R is the external resistance, C is the external capacitance, V is the voltage drop across the resistor and capacitor, $V_L = V - V_s$ is the voltage at the left electrode, and V_s is the driving voltage source.

The electrodes were assumed to be cooled to room temperature $T_w = 293$ K. Zero normal derivatives of all variables were imposed at the side boundaries.

B. Numerical Methods

The conservation laws were solved using approximately-factored, implicit schemes, related to those developed by Beam and Warming,[7] Pulliam,[8] and Surzhikov and Shang.[5] All the calculations were carried out using double-precision arithmetic. Applying the standard transformation from physical coordinates (x, y, z) to grid coordinates (ξ, η, ζ), the conservation equations (1)–(2) can be written in the form:

$$\frac{\partial\overline{U}}{\partial t} + \frac{\partial\overline{E}}{\partial\xi} + \frac{\partial\overline{F}}{\partial\eta} + \frac{\partial\overline{G}}{\partial\zeta} = \frac{\partial\overline{E}_v}{\partial\xi} + \frac{\partial\overline{F}_v}{\partial\eta} + \frac{\partial\overline{G}_v}{\partial\zeta} + \overline{S} \tag{9}$$

where, for example, $\overline{U} = U/J$, $\overline{E} = (\xi_xE + \xi_yF + \xi_zG)/J$, and $U = [n_i, n_e]^T$. (Here J is the Jacobian of the grid transformation.)

Writing Eq. (9) as $\partial\overline{U}/\partial t = R$, and discretizing in time, we have:

$$(1+\theta)\overline{U}^{n+1} - (1+2\theta)\overline{U}^{n} + \theta\overline{U}^{n-1} = \Delta t R^{n+1} \tag{10}$$

where $\theta = 0$ for an implicit Euler scheme and $\theta = 1/2$ for a three point backward scheme. We introduce subiterations such that $\overline{U}^{n+1} \to \overline{U}^{p+1}$, with $\Delta\overline{U} = \overline{U}^{p+1} - \overline{U}^{p}$. The right hand side R^{n+1} is linearized

in the standard 'thin layer' manner. Collecting the implicit terms on the left hand side, and introducing approximate factoring and a subiteration time step $\Delta\hat{t}$ gives an equation set of the form:

$$\mathcal{L}_\xi \mathcal{L}_\eta \mathcal{L}_\zeta \Delta\overline{U} = -\frac{\Delta\hat{t}}{1+\theta}\left\{\frac{(1+\theta)\overline{U}^p - (1+2\theta)\overline{U}^n + \theta\overline{U}^{n-1}}{\Delta t} - R^p\right\} \tag{11}$$

where $\mathcal{L}_\xi$, $\mathcal{L}_\eta$, and $\mathcal{L}_\zeta$ are implicit spatial difference operators.

The drift-diffusion equations were discretized in space using a second-order upwind scheme based on the drift velocity $\mathbf{V}_s = s_s\mu_s\mathbf{E}$. The minmod limiter was employed. A second-order, upwind method was also applied when calculating the species fluxes present in the source terms. (See the discussion of the charged particle generation term in Refs. 5, 9.)

The Poisson equation was also solved using an approximately factored implicit scheme, adapted from the approach described by Holst.[10,11] (The heat conduction equation (6) is solved in an exactly analogous fashion.) Applying the usual transformation of coordinates, the three-dimensional Poisson equation (5) can be written in the form:

$$\frac{\partial\phi}{\partial\tau} = \frac{\partial\overline{E}}{\partial\xi} + \frac{\partial\overline{F}}{\partial\eta} + \frac{\partial\overline{G}}{\partial\zeta} - \overline{S} \tag{12}$$

where the left hand side is an artificial time term that motivates an iterative procedure for driving the right hand side towards zero. We write $\Delta\phi/\Delta\tau = L\phi^{p+1}$, where $\Delta\phi = \phi^{p+1} - \phi^p$. We then linearize the right hand side using the standard 'thin layer' approach, introduce $\alpha = 1/\Delta\tau$, an over-relaxation parameter ω, and approximate factoring. This gives:

$$\mathcal{L}_\xi \mathcal{L}_\eta \mathcal{L}_\zeta \Delta\phi = \omega\alpha^{-1} L\phi^p \tag{13}$$

The spatial derivatives are evaluated using second-order central differences. A cyclic variation of the pseudo-time parameter is used in order to accelerate convergence.

The drift-diffusion equations and the Poisson equation were solved in a loosely-coupled fashion inside a subiteration loop intended to drive $\Delta\overline{U}$ and $\Delta\phi$ toward zero. Typically 3 subiterations were employed, with 10-1000 iterations of the Poisson solver within each overall subiteration. At the end of each RF-cycle, or after each 100 time steps in the DC case, the heat conduction equation was solved using the averaged value of the energy deposition term.

Due to the disparate time scales involved in the diffusive and electromagnetic phenomena occurring in these problems, calculations can be costly in computer time. Efforts have been made to improve the speed of the computations. In the implementation of the factorized schemes, multi-level parallelism is exploited by using vectorization, multi-threading with OpenMP commands,[12] and multi-block decomposition implemented through MPI commands.[13]

III. Results

Numerical calculations were carried out for both DC and RF discharges at pressures of about 5 Torr (670 Pa), with a discharge gap of 2 cm. In particular, the study examined the normal current density effect, in which the discharge accommodates greater current by increasing in cross-sectional area at nearly constant current density.

A. DC Discharges

Two-dimensional calculations of DC glow discharges were carried out first. The test conditions and problem geometry are similar to those considered in Ref. 5. The circuit configuration is as illustrated in Fig. 1, but with a constant $V_s = 2$ kV voltage source. The background pressure was fixed at $p = 670$ Pa, and the wall temperature was taken to be $T_w = 293$ K. Values of the external resistance in the range $R = 200 - 350$ kΩ were considered. The value of the capacitance C was chosen to make the RC time constant about 10 times the time step, where a typical time step was 0.5 ns. The computational domain was taken to be a 20 mm by 40 mm by 20 mm rectangular box. Uniformity was enforced in the z-direction, which always consisted of 5 grid points. All cases were run for more than 10^6 time steps, to a final time of about 0.4 ms.

A grid resolution study was carried out with grids of 35×35, 51×51, 101×101, and 151×151 points. A grid of 101×101 points was found to provide adequate resolution, and was selected for parametric studies.

A finer grid was not found to offer substantial improvement in solution quality, whereas coarser grids tended to overestimate the lateral extent of the discharge and underestimate the charged particle number densities.

Figure 2 shows basic results for the case $R = 300$ kΩ. Number densities are shown in Fig. 2a; the color contours represent the ion density and the solid lines the electron density. The cathode is represented by the left side of the domain ($x = 0$), and anode by the right ($x = 0.02$ m). The cathode spot is quite evident as a peak in the ion number density at the left, and the quasi-neutral positive column can be seen as a region where ion and electron number density contours coincide near the center of the domain.

Contours of electric potential are shown in Fig. 2b, along with selected current lines (trajectories of the current density vector field). The cathode layer and plasma column are seen to distort the electric potential near the center of the domain, where a strong conduction current flows. The strong current and electric field there leads to gas heating, as seen in the temperature contours of Fig. 2c.

The effect of changing external resistance is illustrated in Fig. 3. Profiles of the number densities and potential along the discharge axis are shown in Fig. 3a; the overall number densities are seen to increase with decreasing resistance (increasing discharge current). The cathode potential decreases slightly with increasing current. Numerical results for the different cases are listed in Table 1.

Corresponding temperature profiles are shown in Fig. 3b. As would be expected, the temperature increases with increasing current. Note that the peak temperature occurs toward the left of the domain because of strong heating in the cathode layer.

In order to illustrate the growth of the cathode spot with increasing discharge current, the ion number density contour $n_i = 1.5 \times 10^{15}$ m^{-3} is shown in Fig. 3c for each value of the external resistance. As the external resistance drops and the discharge current increases, the width of the cathode spot increases continuously. The same effect is seen in profiles of the conduction current at the cathode (Fig. 3d).

B. RF Discharges

An additional set of calculations was carried out for RF discharges for a grid and set of test conditions similar to those of the DC discharges. Again, the working gas was nitrogen, and the background pressure was fixed at $p = 670$ Pa with a wall temperature of $T_w = 293$ K. The discharge was driven using a voltage source $V_s = V_0 \cos(2\pi f t)$ with frequency $f = 10$ MHz (period 100 ns), with amplitudes in the range of $V_0 = 450 - 650$ V. The external resistance was chosen as $R = 5$ kΩ and the capacitance as $C = 2$ pF, so that the RC time constant was 10 ns. A typical time step was 0.1 ns, giving 1000 time steps per cycle. The computational domain was taken to be a 20 mm by 40 mm by 20 mm rectangular box, with a $101 \times 101 \times 5$ grid. Uniformity was enforced in the z-direction.

Basic results for the case with $V_0 = 550$ V are shown in Fig. 4 for a time corresponding to the start of a cycle. The presentation follows the same pattern as Fig. 2. Number densities are shown in Fig. 4a; color contours represent ions, black lines electrons. The electrodes lie at the left (driven electrode) and right (grounded electrode) boundaries of the domain. The strong peak in the ion concentration occurring near the electrodes indicates that the discharge state corresponds to the high-current γ-mode, in which secondary emission plays a strong role. Indeed, the similarities of the electrode layers to the cathode layer of the corresponding DC discharge (Fig. 2a) are striking. The instantaneous potential field and current lines in Fig. 4b also resemble the DC results shown in Fig. 2b. Since the temperature distribution reflects the average discharge state, the temperature distribution shown in Fig. 4c is symmetric, in contrast to the DC case (Fig. 2c).

The effects of varying the amplitude of the driving voltage between 450 V and 650 V are illustrated in Table 2 and Fig. 5. The lateral extent (y-direction) of the discharge is illustrated for each case in Fig. 5a through the ion number density contour $n_i = 2 \times 10^{15}$ m^{-3}. Interestingly, the characteristic width of the electrode layers varies to a much greater extent than the width of the plasma column. For the lower voltages, the spanwise (y) extent of the electrode layer is comparable to its axial (x) extent, indicating that the discharge may be in a sub-normal regime.[14]

Corresponding profiles of the root-mean-square, total (conduction plus displacement) current density at the right electrode are shown in Fig. 5b. Note the change in the character of the profile as the driving voltage reaches higher values. Numerical values of the current density are listed in Table 2.

Centerline profiles of number densities and potential are shown in Fig. 5c, with corresponding temperature profiles shown in Fig. 5d. As might be expected, number densities and temperatures increase as the discharge current increases.

IV. Conclusions

As part of an ongoing research effort on plasma actuators for flow control, a numerical study of DC glow discharges and γ-mode RF glow discharges has been carried out. For simplicity, the study focused on two-dimensional problems. Several experimentally observed features of these discharges were reproduced in the numerical computations, including the expansion of the electrode spot with increasing discharge current. These results provide a basic validation of the computer code, but detailed experimental data are needed for true code validation. A corresponding set of axisymmetric calculations is planned for future work.

Acknowledgments

This project is sponsored in part by the Air Force Office of Scientific Research (monitored by J. Schmisseur and F. Fahroo), and by a grant of High Performance Computing time from the Department of Defense Major Shared Resource Center at the Army High Performance Computing Research Center (AHPCRC). The author would like to acknowledge helpful discussions of this ongoing project with I. Adamovich, D. Gaitonde, R. Kimmel, S. Macheret, J. Shang, M. Shneider, and M. White.

References

[1]Raizer, Y. P. and Surzhikov, S. T., "Two-Dimensional Structure in a Normal Glow Discharge and Diffusion Effects in Cathode and Anode Spot Formation," *High Temperature*, Vol. 26, No. 3, 1988, pp. 304–311.

[2]Raizer, Y. P. and Shneider, M. N., "Normal Current Density Effect in RF-Discharge According to Results of Two-Dimensional Numerical Modeling," *IEEE Transactions on Plasma Science*, Vol. 27, No. 3, 1999, pp. 701–706.

[3]Poggie, J., "Computational Studies of High-Speed Flow Control with Weakly-Ionized Plasma," AIAA Paper 2005-0784, American Institute of Aeronautics and Astronautics, Reston VA, January 2005.

[4]Poggie, J., "Plasma-Based Hypersonic Flow Control," AIAA Paper 2006-3567, American Institute of Aeronautics and Astronautics, Reston VA, June 2006.

[5]Surzhikov, S. T. and Shang, J. S., "Two-Component Plasma Model for Two-Dimensional Glow Discharge in Magnetic Field," *Journal of Computational Physics*, Vol. 199, 2004, pp. 437–464.

[6]White, F. M., *Viscous Fluid Flow*, McGraw-Hill, New York, 2nd ed., 1991.

[7]Beam, R. and Warming, R., "An Implicit Factored Scheme for the Compressible Navier-Stokes Equations," *AIAA Journal*, Vol. 16, No. 4, 1978, pp. 393–402.

[8]Pulliam, T. H., "Implicit Finite-Difference Simulations of Three-Dimensional Compressible Flow," *AIAA Journal*, Vol. 18, No. 2, 1980, pp. 159–167.

[9]Poggie, J., "DC Glow Discharges: A Computational Study for Flow Control Applications," AIAA Paper 2005-5303, American Institute of Aeronautics and Astronautics, Reston VA, June 2005.

[10]Holst, T. L., "On Approximate Factorization Schemes for Solving the Full Potential Equation," NASA TM 110435, 1997.

[11]Holst, T. L., "Transonic Flow Computations Using Nonlinear Potential Methods," *Progress in Aerospace Sciences*, Vol. 36, 2000, pp. 1–61.

[12]Chandra, R., Dagum, L., Kohr, D., Maydan, D., McDonald, J., and Menon, R., *Parallel Programming in OpenMP*, Academic Press, San Diego, 2001.

[13]Gropp, W., Lusk, E., and Skjellum, A., *Using MPI: Portable Parallel Programming with the Message-Passing Interface*, The MIT Press, Cambridge, MA, 2nd ed., 1999.

[14]Raizer, Y. P., *Gas Discharge Physics*, Springer, New York, 1991.

R (kΩ)	V_c (V)	$j_{\max}$ (A/m^2)	I (mA)	P (W)	$T_{\max}$ (K)
350	547	32	4.2	2.3	335
300	543	35	4.9	2.7	340
250	539	38	5.8	3.1	346
200	533	42	7.3	3.9	355

Table 1. Two-dimensional DC glow discharge results: external resistance, magnitude of the cathode voltage, maximum cathode current density, net current computed at the anode, power $P = V_c I$ at the cathode, and maximum gas temperature.

V_0 (V)	j_{RMS} (A/m^2)	V_{RMS} (V)	I_{RMS} (mA)	P (W)	$T_{\max}$ (K)
450	31	291	11	0.7	312
475	56	297	14	1.6	329
500	64	305	17	2.3	342
550	78	318	24	4.0	372
600	98	329	33	5.9	400
650	115	339	41	7.9	422

Table 2. Two-dimensional RF glow discharge results: driving voltage, peak total current density, RMS voltage, RMS total current, average power $P = \int_0^T VIdt/T$, maximum gas temperature. Voltages and currents evaluated at left electrode.

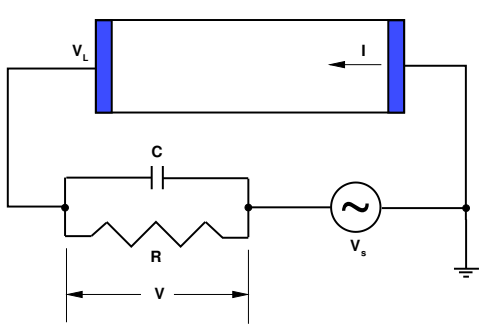

Figure 1. External circuit configuration.

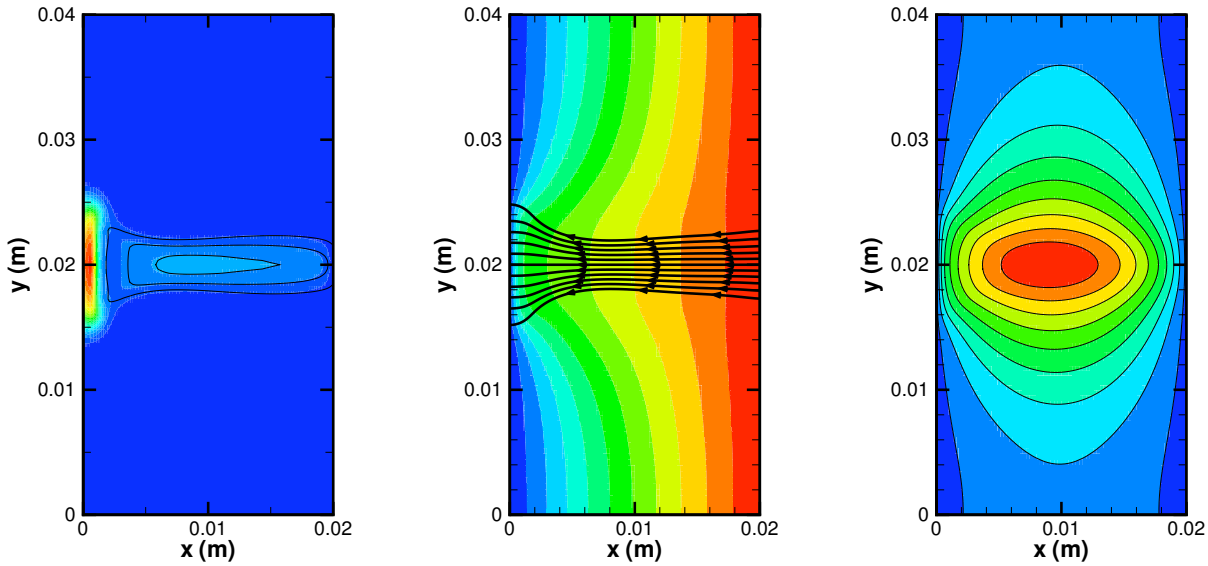

(a) Number densities; contour interval 1×10^{15} m^{-3}.

(b) Electric potential and conduction current lines; contour interval 50 V.

(c) Bulk gas temperature; contour interval 5 K.

Figure 2. Two-dimensional DC glow discharge, $R = 300$ kΩ.

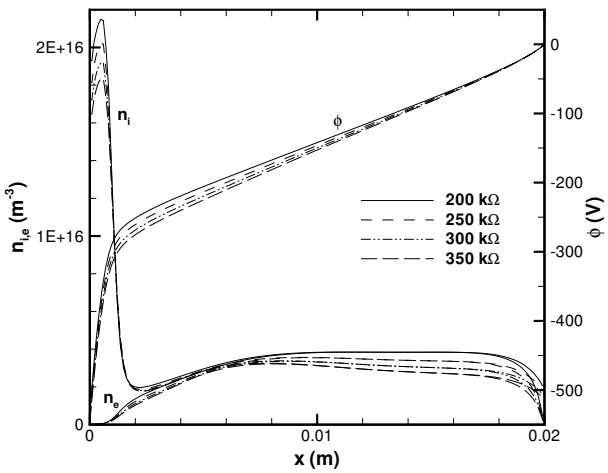

(a) Centerline profiles of potential and number density.

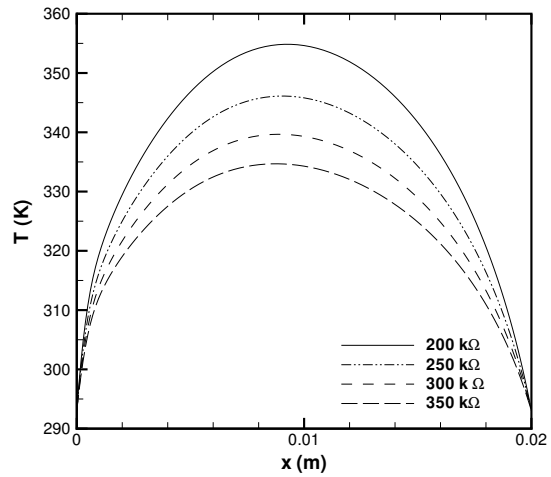

(b) Centerline profile of gas temperature.

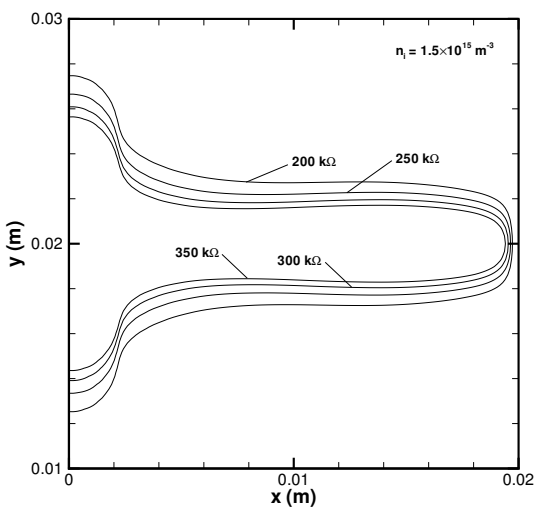

(c) Ion number density contours; $n_i = 1.5 \times 10^{15}$ m^{-3}.

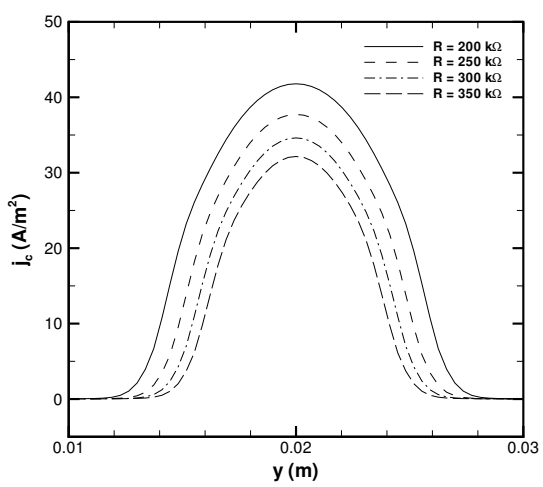

(d) Conduction current density profiles at the cathode.

Figure 3. Two-dimensional DC glow discharge, $R = 200 - 350$ kΩ.

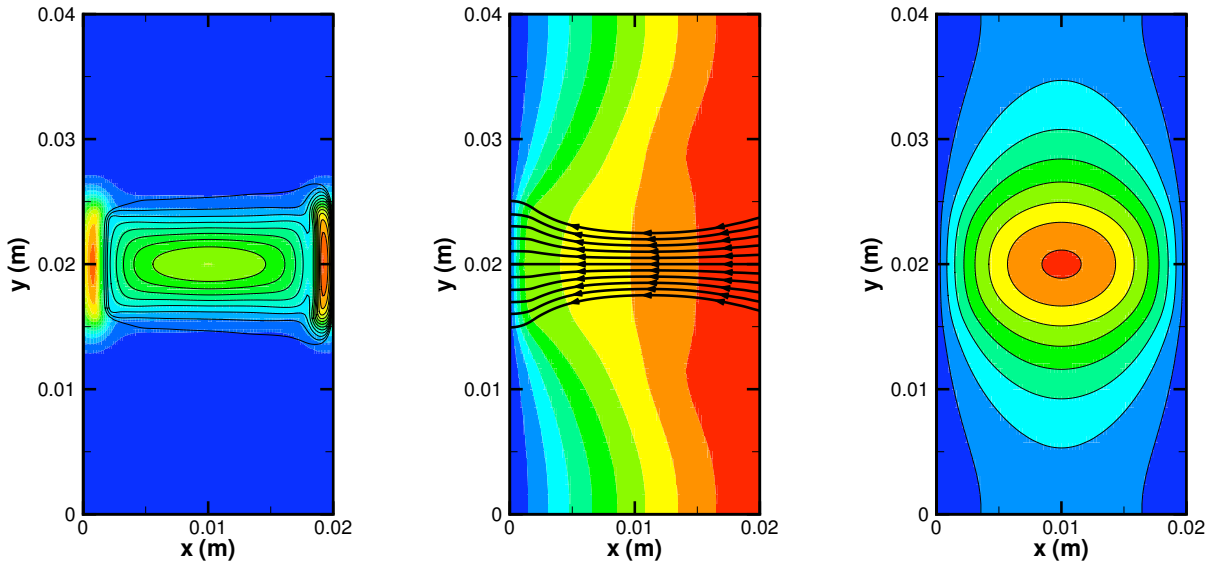

(a) Number densities; contour interval 1×10^{15} m^{-3}.

(b) Electric Potential and conduction current lines; contour interval 50 V.

(c) Bulk gas temperature; contour interval 10 K.

Figure 4. Two-dimensional RF glow discharge at 0% phase, $V = 550$ V, $f = 10$ MHz, $R = 5$ kΩ, $C = 2$ pF.

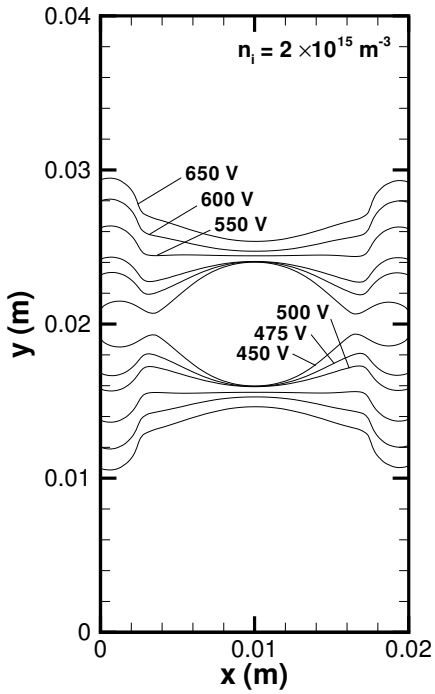

(a) Ion number density contours; $n_i = 2 \times 10^{15}$ m^{-3}.

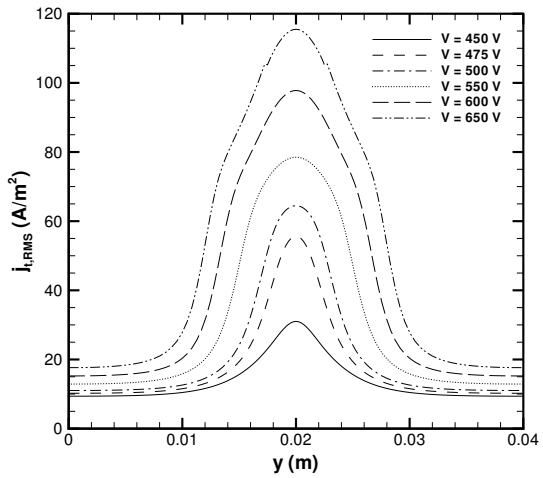

(b) Cycle-averaged, RMS, total current density profiles at the right electrode.

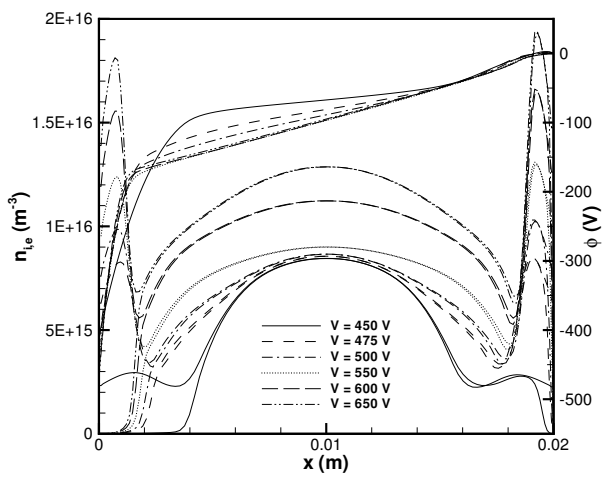

(c) Centerline profiles of potential and number density.

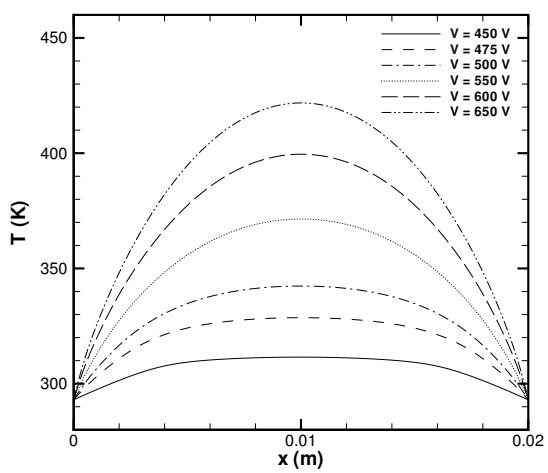

(d) Centerline profile of temperature.

Figure 5. Two-dimensional RF glow discharge, $V = 400 - 650$ V, $f = 10$ MHz, $R = 5$ kΩ, $C = 2$ pF.